Case C1.2: Transonic Ringleb Flow

Masayuki Yano* and David L. Darmofal†

Aerospace Computational Design Laboratory, Massachusetts Institute of Technology

I. Code Description

ProjectX is a high-order, adaptive discontinuous Galerkin finite element solver. The DG discretization uses Roe's approximate Riemann solver[1] for the inviscid numerical flux. The solution to the discretized system is obtained using a Newton-based nonlinear solver with pseudo-time continuation; however, due to the simplicity of this case, we employ a very high CFL number (10^6) to achieve near-Newton convergence. The linear system arising in each pseudo-time step is solved using GMRES,[2] preconditioned with an in-place block-ILU(0) factorization[3] with minimum discarded fill reordering and $p = 0$ algebraic coarse correction.[4]

An output-based, anisotropic simplex mesh adaptation algorithm is used to control the discretization error.[5] The algorithm iterates toward a mesh that minimizes the output error for a given number of degrees of freedom. The anisotropic adaptation decisions are entirely driven by the behavior of an output-based *a posteriori* error estimate; thus, the method handles any discretization order, naturally incorporates both the primal and adjoint solution behaviors, and robustly treats irregular features. The output error estimate uses the dual-weighted residual (DWR) method of Becker and Rannacher.[6] A new mesh that conforms to the metric request is generated using using BAMG (Bidimensional Anisotropic Mesh Generator),[7] and higher-order, globally curved meshes are constructed through linear elasticity.[8]

II. Case Description

II.A. Flow Condition

This case considers transonic Ringleb flow. The boundary fluxes at the inflow, outflow, and walls are determined using the Roe's approximate Riemann solver in which the exterior state is set to the analytical solution.

II.B. Convergence Criterion

The ℓ^2 norm of the DG residual of non-dimensionalized Navier-Stokes equations is used to monitor convergence to the steady state. Our solver operates on non-dimensionalized variables

$$\rho^* = \frac{\rho}{\rho_\infty}, \quad u^* = \frac{u}{\|V_\infty\|}, \quad v^* = \frac{u}{\|V_\infty\|}, \quad p^* = \frac{p}{\rho_\infty \|V_\infty\|^2}, \quad e^* = \frac{e}{\|V_\infty\|^2},$$
$$R^* = \frac{R}{c_v}, \quad T^* = \frac{T}{\|V_\infty\|^2/c_v}, \quad \text{and} \quad \mu^* = \frac{\mu}{\rho_\infty L_\infty V_\infty}.$$

The DG residual is computed against the Lagrange test functions with equidistributed nodes, and the ℓ^2 norm of the residual is converged to 1×10^{-9}. (Note that the solver time would not be significantly influenced for any reasonable choice of the tolerance (say $< 1 \times 10^{-7}$), as we achieve Newton convergence in this regime. With the specified non-dimensionalization, the difference between the ℓ^2 residual and the mass residual is well within this offset.)

*Doctoral candidate, 77 Massachusetts Ave. 37-442, Cambridge, MA, 02139, myano@mit.edu

†Professor, 77 Massachusetts Ave. 37-451, Cambridge, MA, 02139, darmofal@mit.edu

II.C. Hardware Specification

All computations are performed in serial on a Linux machine with an Intel i7-2600 processor and 16 Gbytes of RAM. The machine produces a Taubench time of 6.60 seconds.

II.D. Residual Timing

The time for performing a single dof $= 250,000$ residual evaluation, including the full Jacobian for the implicit solver, is summarized in Table 1. The residual evaluation is performed on a 11,116-element mesh and the times are scaled to 250,000 degrees of freedom. Note that residual evaluation is faster than in the C1.1 bump case, as the $q = 3$ geometry representation, as oppose to the $q = 5$ representation, is used for this case, which warrants the use of a lower order quadrature rule for a given p.

p	time (work unit)
1	0.69
2	0.57
3	0.69

Table 1. dof $= 250,000$ residual evaluation time (including the full Jacobian construction).

II.E. Initial Mesh

The initial mesh used for this case is shown in Figure 1. The curved geometry is represented using $q = 3$ simplex elements. After each mesh refinement, the geometry representation is refined by re-sampling from the analytical geometry definition.

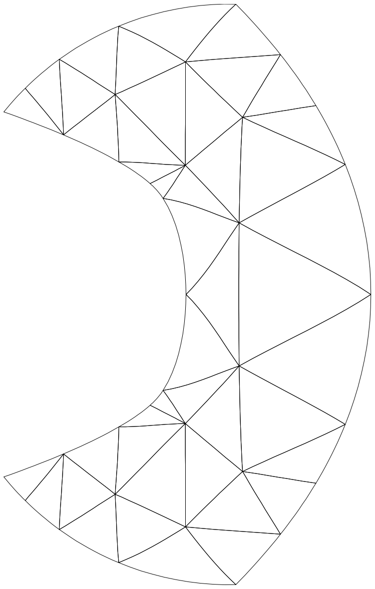

Figure 1. The initial 44-element mesh.

II.F. Adaptation Procedure and Data Reported

For this case, the ranges of the solution orders, p, and the number of degrees of freedom, dof, considered are

$$p \in \{1, 2, 3\} \quad \text{and} \quad \text{dof} \in \{500, 1000, 2000, 4000, 8000\}.$$

For each p-dof combination, a family of optimized meshes are generated using our anisotropic simplex adaptation algorithm.[5] The output adapted, J, is the difference in the local and freestream entropy measured in the L^2 norm (squared), i.e.

$$J = \int_\Omega \left(\frac{p}{\rho^\gamma} - \frac{p_\infty}{\rho_\infty^\gamma} \right)^2 dx,$$

where p is pressure, ρ is density, p_∞ is the freestream pressure, ρ_∞ is the freestream density, and $\gamma = 1.4$ is the ratio of specific heats.

As in Case 1.1, the performance of each p-dof is assessed by averaging the error obtained on five realization of meshes in the family. The time reported is the total time required to reach the first realization of the p-dof-optimized mesh starting from the initial mesh shown in Figure 1; this includes multiple flow solves and adaptation overhead. See the description provided in Case 1.1 for details of the adaptation procedure.

III. Results

III.A. Error Convergence

Figure 2(a) shows the convergence of the L^2 norm of the entropy error normalized by the domain area,

$$\mathcal{E}_{\text{ent}} = \sqrt{\frac{1}{|\Omega|} \int_\Omega \left(\frac{p/\rho^\gamma - p_\infty/\rho_\infty^\gamma}{p_\infty/\rho_\infty^\gamma} \right)^2 dx},$$

against the number of degrees of freedom, dof. For this smooth problem, the expected convergence rate of the L^2 norm of the entropy error is

$$\mathcal{E}_{\text{ent}} = C h^{p+1} = \tilde{C} (\text{dof})^{-\frac{p+1}{2}}. \qquad (1)$$

In particular, for $p = 1$, 2, and 3, the theoretical convergence rate against (dof) is 1, 1.5, and 2, respectively. The figure shows that all discretization orders produce the optimal convergence rate. Note that, because the flow is smooth, adaptive refinement is unnecessary to achieve the optimal convergence rate. However, adaptation does reduce the values of error for a given degrees of freedom, i.e. adaptation decreases the value of the constant C (or $\tilde{C}$) in the error expression Eq (1). In general, $p > 1$ discretizations are more efficient than the $p = 1$ discretization both in terms of the degrees of freedom (Figure 2(a)) and time (Figure 2(b)).

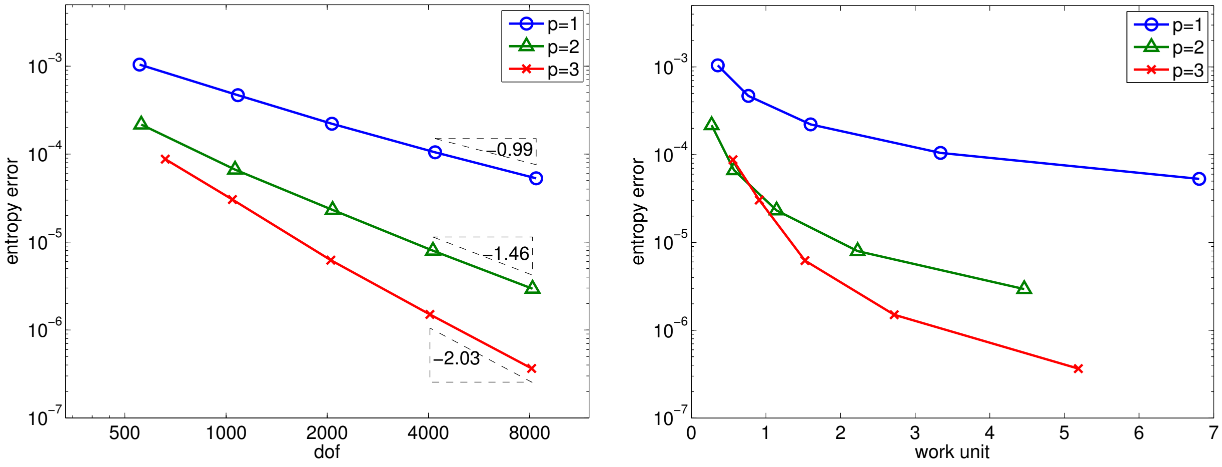

(a) entropy error vs. dof

(b) entropy error vs. work unit

Figure 2. L^2 entropy error convergence.

III.B. Comparison of Adapted Meshes

The entropy error adapted meshes obtained for select p-dof combinations are shown in Figure 3 and 4. In general, the adaptive refinement targets the inner wall, in particular near the kinks. However, the element-size grading is weak as the flow features are smooth. Even though an anisotropic adaptation algorithm is employed, the resulting meshes are mostly isotropic due to the absence of anisotropic flow features.

Figure 3 shows $p = 1$, 2, and 3 meshes with the error level of approximately 5×10^{-5}. The $p > 1$ discretizations require significantly fewer number of elements to achieve this error level.

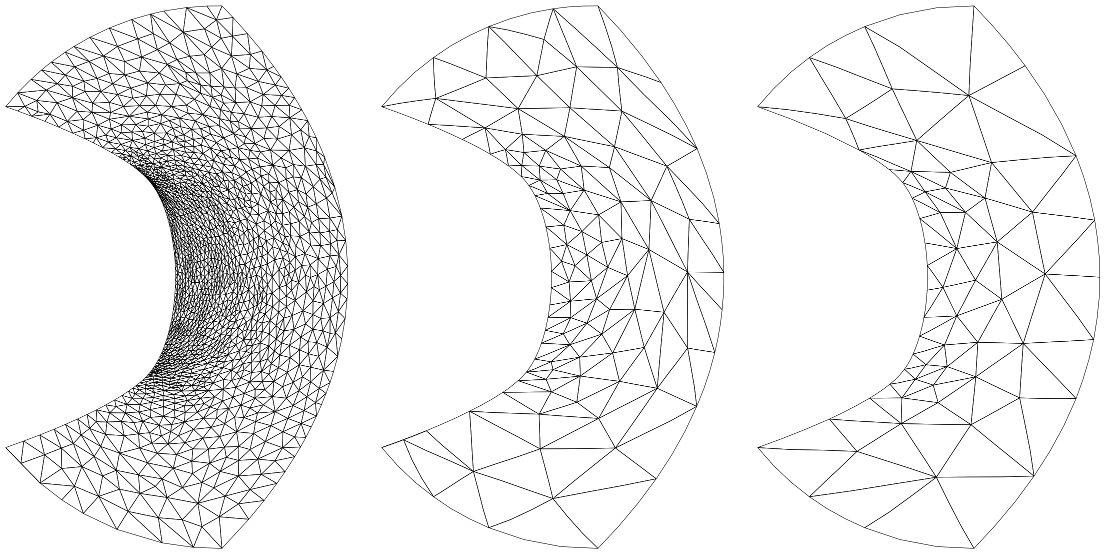

(a) $p = 1$, dof $= 8,000$, $\mathcal{E} = 5.3 \times 10^{-5}$

(b) $p = 2$, dof $= 1,000$, $\mathcal{E} = 6.7 \times 10^{-5}$

(c) $p = 3$, dof $= 1,000$, $\mathcal{E} = 3.0 \times 10^{-5}$

Figure 3. Select $p = 1$, 2, and 3 entropy-adapted meshes with a similar error level.

Figure 4 shows three $p = 3$ meshes with increasing numbers of degrees of freedom, illustrating how the mesh evolves for a fixed p to achieve a lower error level. As the flow is smooth, the refinement is mostly uniform.

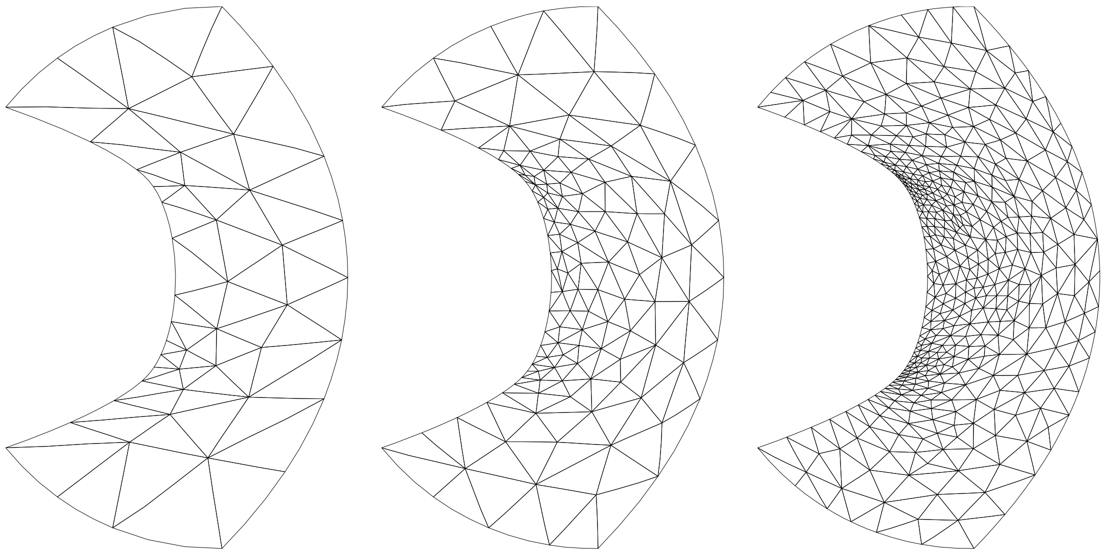

(a) $p = 3$, dof $= 500$, $\mathcal{E} = 8.7 \times 10^{-5}$

(b) $p = 3$, dof $= 2,000$, $\mathcal{E} = 6.2 \times 10^{-6}$

(c) $p = 3$, dof $= 8,000$, $\mathcal{E} = 3.7 \times 10^{-7}$

Figure 4. Select $p = 3$ entropy-adapted meshes with increasing numbers of degree of freedom.

III.C. Uniform vs. Adaptive Refinement

Figure 5 shows the convergence results obtained using adaptive refinement and a step of uniform refinement starting from select adapted meshes. As the problem is smooth, optimal convergence rate is obtained using either uniform or adaptive refinement. However, this does not mean that adaptation does not affect the accuracy of the solution; the constant C of the error $\mathcal{E} = C(\text{dof})^{-\frac{p+1}{2}}$ is affected even for this simple problem. The result merely suggests that once an optimal element size distribution is determined, then uniform refinement from the optimized configuration is sufficient to maintain the optimal error level. (See Case 1.1 on the difference between a step of uniform refinement starting from an adapted mesh and truly uniform mesh.)

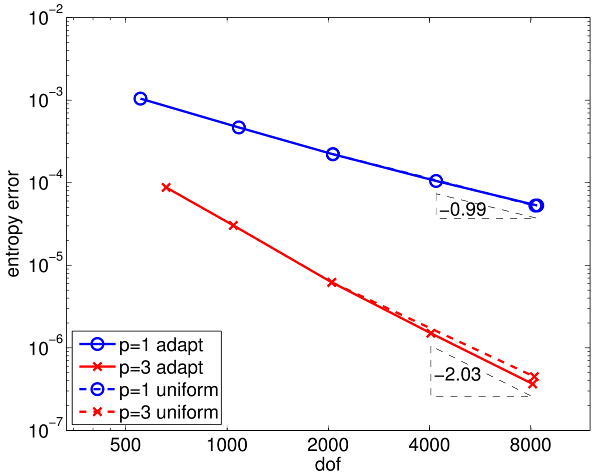

Figure 5. Comparison of adaptive refinement and uniform refinement starting from adapted meshes.

Figure 6 shows the timing breakdown of the adaptation overhead relative to the primal solve (i.e. the flow solve). Due to the small problem size and the ease of converging the primal problem, adaptation overhead is significant for this problem.

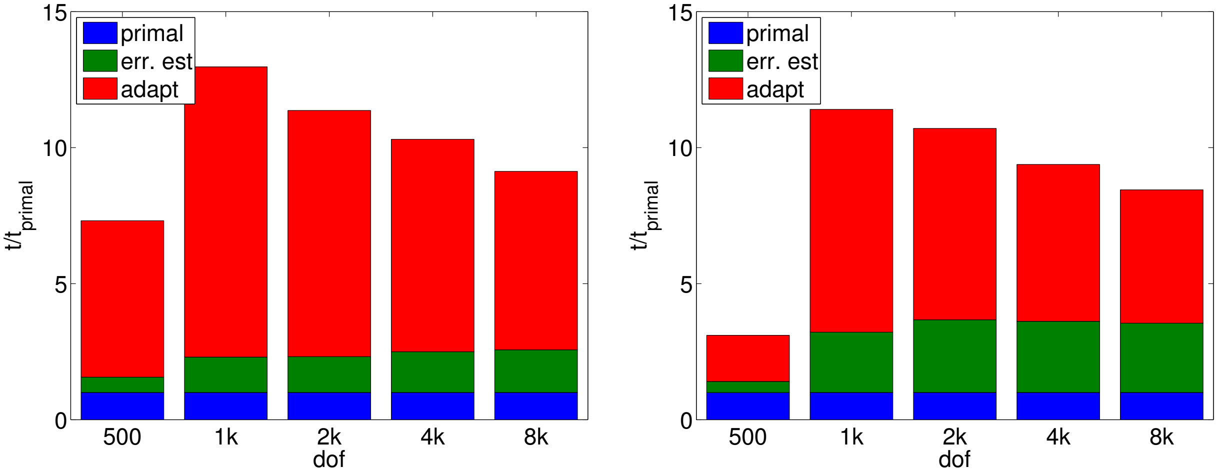

(a) $p = 1$ (b) $p = 3$

Figure 6. Timing breakdown.

Acknowledgments

The authors would like to thank the entire ProjectX team for the many contributions that enabled this work. This work was supported by the Singapore-MIT Alliance Fellowship in Computational Engineering and The Boeing Company with technical monitor Dr. Mori Mani.

A. Comparison of Exact and Inviscid-Wall BCs

As described in the flow condition description in Section II.A, the results in Section III were obtained by specifying the boundary fluxes at the inflow, outflow, and walls using the Roe's approximate Riemann solver with the exterior state set to the analytical solution. This section provides a short summary of the change in the solver behavior when the boundary conditions at the inner and outer walls are replaced by flow tangency conditions.

In terms of robustness, obtaining the steady state solution becomes difficult when the flow tangency conditions are imposed on the walls. The convergence difficulty arise from the formation of an artificial shock on the inner wall of the compression region. In order to prevent the formation of the artificial shock, the solver must not only accurately capture the geometry but also accurately capture the compression waves with minimal dissipation. In particular, we were unable to reliably obtain a steady state solution using the configurations that would result in the area-normalized L^2 entropy error of larger than 10^{-5}. (Note that "reliability" in the context adaptation means finding the solution on every mesh encountered in the adaptive sequence without a single failure.) Consequently, the $p = 1$ discretization could not find a steady state solution using a reasonable number of degrees of freedom. The lack of convergence is not simply due to the geometry representation, as the combination of a higher-order geometry representation ($q = 5$) and high-order quadrature rules (24th order on the faces and 15th order on the volumes) does not solve the problem for the $p = 1$ discretization.

Figure 7 compares the behaviors of the area-normalized L^2 entropy error for the exact and inviscid-wall boundary conditions. Each p-dof combination is optimized using our adaptation algorithm, and the average error of five realizations of a particular p-dof combination is reported. Note that the meshes for the exact and inviscid-wall BC cases are different from each other; nevertheless, the optimal meshes for the inviscid-wall BC cases are very similar to those for the exact BC cases, e.g. shown in Figure 4. For the cases with inviscid-wall BCs, only those p-dof combinations that can be solved reliably is reported; as mentioned above, this roughly corresponds to configurations that results in the entropy error of less than 10^{-5}. The inviscid-wall boundary condition results in a slightly higher error compared to the exact state, but the error convergence behaviors are very similar. Thus, the primary difference in the two boundary conditions is the degree of difficulty in finding the steady state solution.

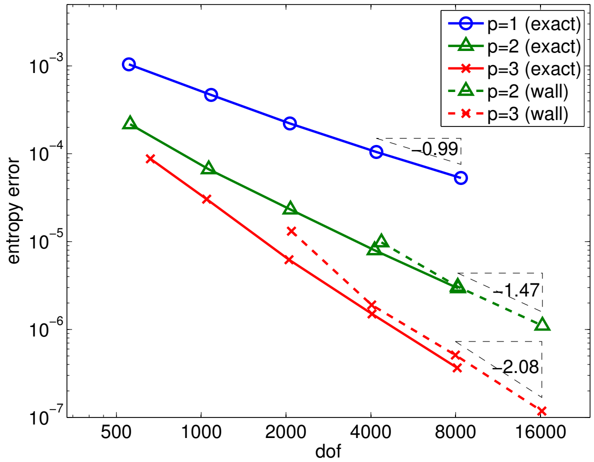

Figure 7. Comparison of the entropy error convergence for the exact and inviscid-wall boundary conditions.

References

[1] P. L. Roe, Approximate Riemann solvers, parameter vectors, and difference schemes, J. Comput. Phys. 43 (2) (1981) 357–372.

[2] Y. Saad, M. H. Schultz, GMRES: A generalized minimal residual algorithm for solving nonsymmetric linear systems, SIAM Journal on Scientific and Statistical Computing 7 (3) (1986) 856–869.

[3] L. T. Diosady, D. L. Darmofal, Preconditioning methods for discontinuous Galerkin solutions of the Navier-Stokes equations, J. Comput. Phys. 228 (2009) 3917–3935.

[4] P.-O. Persson, J. Peraire, Newton-GMRES preconditioning for discontinuous Galerkin discretizations of the Navier-Stokes equations, SIAM J. Sci. Comput. 30 (6) (2008) 2709–2722.

[5] M. Yano, D. Darmofal, An optimization framework for anisotropic simplex mesh adaptation: application to aerodynamic flows, AIAA 2012–0079 (Jan. 2012).

[6] R. Becker, R. Rannacher, An optimal control approach to a posteriori error estimation in finite element methods, in: A. Iserles (Ed.), Acta Numerica, Cambridge University Press, 2001.

[7] F. Hecht, Bamg: Bidimensional anisotropic mesh generator,
http://www-rocq1.inria.fr/gamma/cdrom/www/bamg/eng.htm (1998).

[8] T. A. Oliver, A higher-order, adaptive, discontinuous Galerkin finite element method for the Reynolds-averaged Navier-Stokes equations, PhD thesis, Massachusetts Institute of Technology, Department of Aeronautics and Astronautics (Jun. 2008).